Ablation and Spallation of Metals by Femtosecond Laser Pulse

N.A. Inogamov[1,a], V.V. Zhakhovsky[2,3,b], S.I. Ashitkov[3,c], V.A. Khokhlov[1,d], B.J. Demaske[2,e], S.I. Anisimov[1,f], M.B. Agranat[3,g], V.E. Fortov[3,h], and I.I. Oleynik[2,i],

[1] Landau Institute for Theoretical Physics, Russian Academy of Sciences, Chernogolovka, Moscow region, 142432, Russian Federation

[2] Department of Physics, University of South Florida, Tampa, Florida 33620, USA

[3] Joint Institute for High Temperatures, Russian Academy of Sciences, Moscow, 125412, Russian Federation

[a] nailinogamov@gmail.com, [b] vasily@usf.edu, [c] Ashitkov11@yandex.ru, [d] v_a_kh@mail.ru, [e] bdemaske@mail.usf.edu, [f] anisimov@itp.ac.ru, [g] agranat2004@mail.ru, [h] fortov@ihed.ras.ru, [i] oleynik@usf.edu

Keywords: ablation, spallation, nanoablation and nanospallation by optical short pulse lasers

Abstract. Irradiation of metals by femtosecond (fs) laser pulse causes pressure buildup within a thin surface layer of thickness d_T in the range 50-200 nm depending on particular metal. As a result, an acoustic wave, consisting of a compressive wave front and rarefaction tail, forms propagating into the bulk. Such a two-part wave with positive and negative pressure parts is generated during acoustic decay of the pressurized layer followed by reflection of acoustic wave from the free vacuum boundary. Elapsed time for creation of the two-part pressure wave $t_s \sim d_T / c_s \sim 10-50$ ps, where c_s is speed of sound. Stretching due to the negative pressure of the two-part wave can cause detachment and run away (ejection, spallation) of a layer of condensed metal from the target if the tensile stress exceeds the metal's dynamical strength σ^*, which depends on the metal temperature and strain rate produced by the wave. In laser physics this phenomenon is called thermo-mechanical ablation. Simulations of aluminum, gold and nickel targets show that for $\sigma > \sigma^*$ the surface layer is in molten state after laser energy absorption. Strong tensile stress in negative pressure wave results in bubble nucleation in a hot molten layer. This phenomenon is called cavitation. Cavitation is followed by inertial expansion into vacuum of a liquid-vapor mixture accelerated by rarefaction wave. Corresponding motion of the free surface is observed in fs laser experiments. The experimental tensile strength is obtained from the decrease in velocity during deceleration of the ejected layer. Simulations show a temperature dependence of the tensile strength $\sigma^*(T)$ for liquid metals that agrees well with experimental data.

As the two-part pressure wave propagates into the bulk, the positive pressure wave transforms to a shock due to nonlinearity of the compression wave resulting in focusing of characteristics. In the

case of a free-standing metal film, the shock wave is reflected from the rear-side and, if the tensile strength of the reflected wave exceeds the dynamical spall strength of the solid metal, causes spallation. Thus, the tensile strengths for both molten and solid phases are obtained for several metals from fs laser experiments and simulation.

Thickness d_T and sonic time t_s are extremely small in comparison with scales for more usual flyer plate impact experiments and experiments with nanosecond (ns) lasers. Therefore our measurements of strengths correspond to very high strain rates $\dot{V}/V$ in the range ~10^9 s^{-1}, approaching ideal or limiting strength. E.g., the strengths for Al are of the order of few GPa. Our laser pump-probe diagnostic technique has time resolution, which is 2-3 orders of magnitude higher than more usual VISAR, ORVIS technique used in flyer plate impact and ns laser experiments.

Authors (NAI, SIAsh, VAK, SIAn, MBA) acknowledge the support from RFBR grant No. 10-02-00434-a.

Introduction

We consider action of a single short pulse onto non-transparent target like metal. Short means that duration of a pulse is shorter than acoustic time scale $\tau_L < t_s = d_T / c_s$; in our cases there is $\tau_L \sim 0.01-1$ ps. Result of laser action depends on absorbed fluence F_{abs} (energy per unit of square) and thickness of target d_{film}, see Fig. 1. Fluence F_{abs} is plotted as the dashed horizontal axis in Fig. 1. Heating by pulse causes expansion of matter. Therefore for $F_{abs} > 0$ the boundary of target deviates from its position $x = 0$ prior to pulse action. This deviation at a fixed time instant increases as fluence increases. At a melting threshold F_m a molten layer appears near the irradiated surface 1. Melt occupies layer between the boundary 1 and the melting front 2, see Fig. 1.

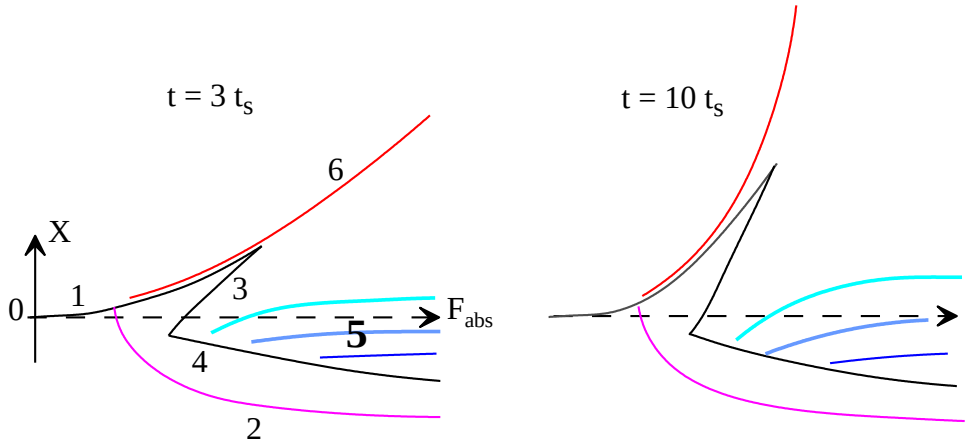

Fig. 1. Role of laser energy: from low to high energy from left to right along the horizontal axis F_{abs}. Left and right pictures correspond to different time instants. 1 is a border of condensed matter; 2 is a melting front; 3 is an upper boundary of a cavitation layer. For fixed F_{abs} and instant of time after nucleation, this is a plane layer under the surface 1. Its upper and bottom boundaries are the surfaces 3 and 4. 5 is a low velocity dense foam region near the bottom 4 of the cavitation layer. 6 is an upper boundary of a vapor cloud. Initial position of the target-vacuum boundary is the dashed line 1. Nucleation begins after time $\cong t_s$ after irradiation by short pulse.

Above the ablation threshold F_{abl} a cavitation layer and correspondingly the surfaces 3 and 4 in Fig. 1 appear. Expansion velocities are larger for higher energies. Therefore spatial separation of surfaces

3 and 4 increases with F_{abs}. Thickness of thermally and dynamically affected layer enlarges with time – compare the left and right parts of Fig. 1.

Temperature and expansion velocity of an outer part of a laser plume increase with energy F_{abs}. While temperature of the bottom part of thermally affected layer always is of the order of melting temperature prior to reverse of melting front and beginning of recrystallization. Therefore differences in thermodynamic state and velocities between the upper plume in Fig. 1 and the bottom become wider at higher F_{abs}. Liquid spallation plate disappears at an "evaporation" threshold $F_{ev} \sim 2F_{abl}$ where the surfaces 1 and 3 in Fig. 1 merge. For metals the melting threshold is significantly below the ablation threshold $F_m \sim (0.3-0.5)F_{abl}$. Typical for ablation thresholds are values $F_{abl} \sim 0.1$ J/cm^2. In case F_{abs} of the order of few J/cm^2 $\sim (10-30)F_{abl}$ the pressures at the time interval $\tau_L < t < t_{eq}$ achieve Megabar values [1,2] inside a thin layer of condensed matter; here t_{eq} is electron and ion temperatures equilibration time; laser pulse with duration $\tau_L < t_{eq}$ heats electron subsystem to temperatures which are much higher than ion temperature at the end of the pulse.

At high energies $F_{abs} \sim 10$ kJ/cm^2 and intensities $\sim 10^{17}$ W/cm^2 peoples mainly study the X-ray flash generated by short pulse laser irradiation. They do not pay significant attention to the phenomena at the relatively cold bottom of the heat affected layer. But in the case of thick enough targets, these phenomena of course exist. Film thickness d_{film} cuts a range of temperatures in the plume from its hot plasma upper edge to the relatively cold bottom below, see Fig. 1. At very high intensities $\sim 10^{21}$ W/cm^2, achieved today at the petawatt laser facilities, peoples concentrate on ultra relativistic electrons and ion acceleration. Below we restrict ourselves to the interval of moderate fluencies near the ablation threshold F_{abl}. This interval is interesting for many technological and biological applications.

Statement of problem

There are three combinations of directions of pump beam arrival versus positions of metal film supported by a glass window. They are shown in Fig. 2. Thickness of glass plate ~100 microns is much larger than thickness (d_{film}~0.1-10 microns) of a film. The middle and the right configurations in Fig. 2 are necessary to study frontal motions shown in Fig. 1. Rear-side spallation into vacuum may take place (if stress σ overcomes material strength σ^*) in the left and in the right cases.

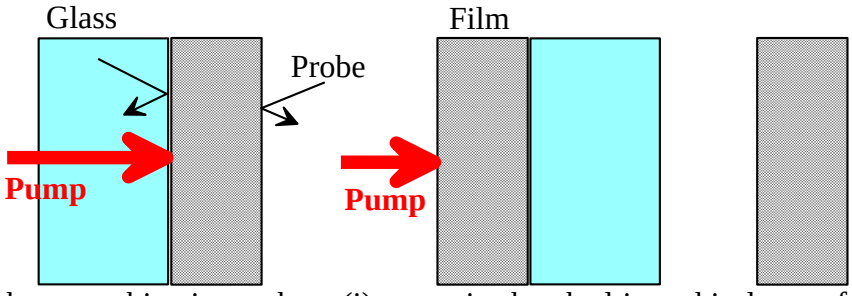

Fig. 2. There are three combinations where (i) pump is absorbed in a skin-layer of metal film after propagating through glass substrate; (ii) the frontal side of a film is a boundary with air or vacuum; (iii) freestanding film. Probe laser follows the expansion of frontal or rear-side boundary of a film.

The right case shown in Fig. 2 is rarely used in our experiments [3,4]. Point is that for the pump-probe micro interferometric (MI) measurements many shots in different equivalent positions of a target are necessary (shots differ in delay time between pump and probe [3,4]). There is a plate with small holes. Diameter of holes is ~1 mm. Every hole is covered by thin (d_{film}~micron) freestanding film. First of all it is difficult to fabricate such target. And also, freestanding film, attached to the hole, bends around an irradiated spot in the direction of pump beam. Creation of momentum by an ablation plume is the reason of bending. Diameter of an irradiated spot is of several tens of microns. Bending makes difficult to obtain final MI images. These images are used to estimate residual deformations in the region of an irradiated spot.

We have studied rear-side reflection of a pressure wave created by irradiation of a glass-metal boundary through glass (the left configuration in Fig. 2) [3-5]. It turned out that it is difficult to achieve material strength σ^* in a pressure wave initiated by pump. The glass window prevents increasing of fluence absorbed in metal. Optical breakdown of glass begins at the boundary with metal. Threshold for this breakdown F_{opt} is lower than the threshold for bulk glass. The threshold F_{opt} limits amount of energy $F_{abs}^{\lim}$ delivered into metal.

Metals with high reflection (e.g., Al) absorb less than metals with higher absorption (e.g., Fe). Also in case with high reflection total electric field (incident together with reflected) near glass-metal boundary is larger, while changes of F_{opt} are relatively weak for similar glasses. Therefore value $F_{abs}^{\lim}$ is smaller in case of high reflection: $F_{abs}^{\lim}$ for Al is smaller than $F_{abs}^{\lim}$ for Fe, Ni. But the strengths σ^* of Fe or Ni are larger in comparison with Al. Our experiments show that interplay between $F_{abs}^{\lim}$ and σ^* allows to achieve only the interval of fluencies near the spallation threshold F_{spall} for Al [3-5] with $F_{abs} \cong 130$ mJ/cm^2. More strong metals (Ni, Fe, Ta) remain continuous after reflection of laser shock from the rear-side boundary shown in the left part of Fig. 2. Simulations show that typical ratio between spallation and ablation thresholds (for the order of micron thick films) is ~(1.5-2) [6, 7]. Spallation threshold is higher because metal at the rear-side is in solid state and because compression wave slowly decays during propagation through film.

We should emphasize that above we discuss spallation but not a process of detachment of metal film from a glass substrate. During the process of spallation the cracks and voids appear at some distance $d_{spall}(F_{spall}, d_{film})$ from a rear-side. This is a thickness of a spallation plate at a spallation threshold F_{spall}. The distance d_{spall} is defined by thickness of a compression wave [5-7]. Above threshold the function $d_{spall}(F, d_{film})$ depends on amplitude of shock arriving at a rear-side. The shock amplitude is defined by fluence and distance d_{film} traveled by shock. Of course, there is competitive process of separation of metal film as whole from the glass support. Separation may take place due to breaks of adhesive bonds between glass and metal. In future, using of different support plate (e.g., sapphire) seems to be attractive because of higher optical breakdown threshold and different adhesion.

Influence of glass on absorption

Fig. 3 shows dependence of absorption coefficient on incident fluence. Pump beam illuminates target at normal angle. The lines 1, 3 and 3a correspond to a linear absorption (Fresnel approximation) for the case of air-Al surface (the line 1) and for the case of air-glass-Al sandwich (the lines 3 and 3a). The case of an air-glass-Al sandwich is shown in Fig. 2 (the left part of Fig. 2).

Refraction coefficients for the first harmonics of Ti:sapp laser ($\lambda = 800$ nm) are 1.5 (glass) and 2.8+8.45i (Al). The line 3a corresponds to the single reflection from the air-glass-Al sandwich, while the line 3 is higher because it includes multiple reflections in a glass plate.

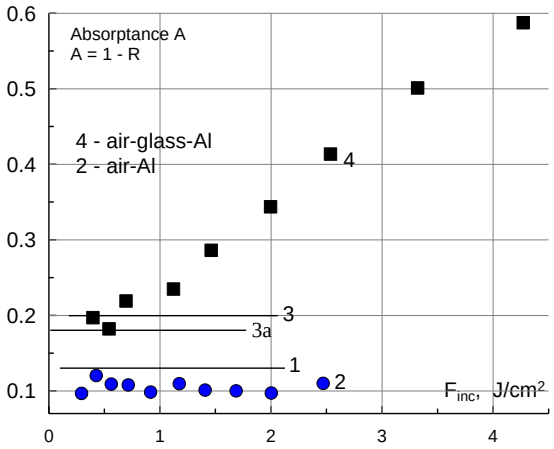

Fig. 3. Optical breakdown at glass-metal interface and increase of absorption A. Black squares 4 correspond to the left case shown in Fig. 2; blue circles 2 show absorption in the middle and right cases shown in Fig. 2. The line 1 presents coefficient A calculated from Fresnel formulas for air-aluminum interface (linear absorption). The lines 3 and 3a corresponds to linear absorption in the left case shown in Fig. 2. As result of breakdown non-linear absorption appears, and experimental black squares 4 begin to deviate from the lines 3 and 3a.

At incident fluence ~(1-1.3) J/cm^2 absorption in the air-glass-Al sandwich begins to deviate from a linear law. This indicates that part of light energy is absorbed in glass as result of optical breakdown of glass. The glass plate works as a non-linear shutter. Above breakdown threshold, it transmits only an initial part of a pump pulse and cuts off subsequent part of pump, see Fig. 4. As was said above, this limits amount of energy, which may be delivered to the Al surface, for the pump with these particular values of wavelength and duration. At the same fluencies, the air-Al surface continues to absorb in linear regime – the blue circles 2 n Fig. 3 do not deviate from Fresnel law (the line 1).

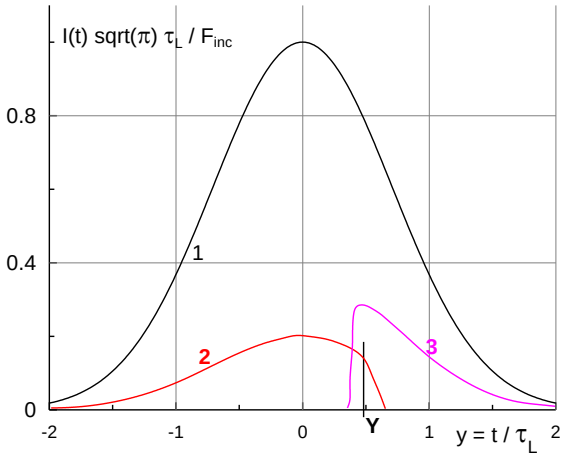

Fig. 4. The Gaussian shape of an incident pump pulse 1. The curves 2 and 3 show intensities of absorption in Al (the curve 2) and in glass (the curve 3). Time is normalized respective to pump duration. The case above an optical breakdown threshold is shown.

Power, which drives hydrodynamic motion inside a metal film, significantly depends on physics of optical breakdown in glass in case of subnanosecond laser pulses used [8, 9] to drive shock in metal film in the left configuration shown in Fig. 2. Breakdown very seriously cuts mechanical efficiency of laser pulse. Compare curves 1 and 2 in Fig. 4 to understand this.

Generation of compression wave

Melting, expansion and formation of compression wave at a glass-Al boundary are shown in Fig. 5. Initial position of this boundary is $x=0$. Two-temperature model, used for this hydrodynamic simulation, is described in [10-12].

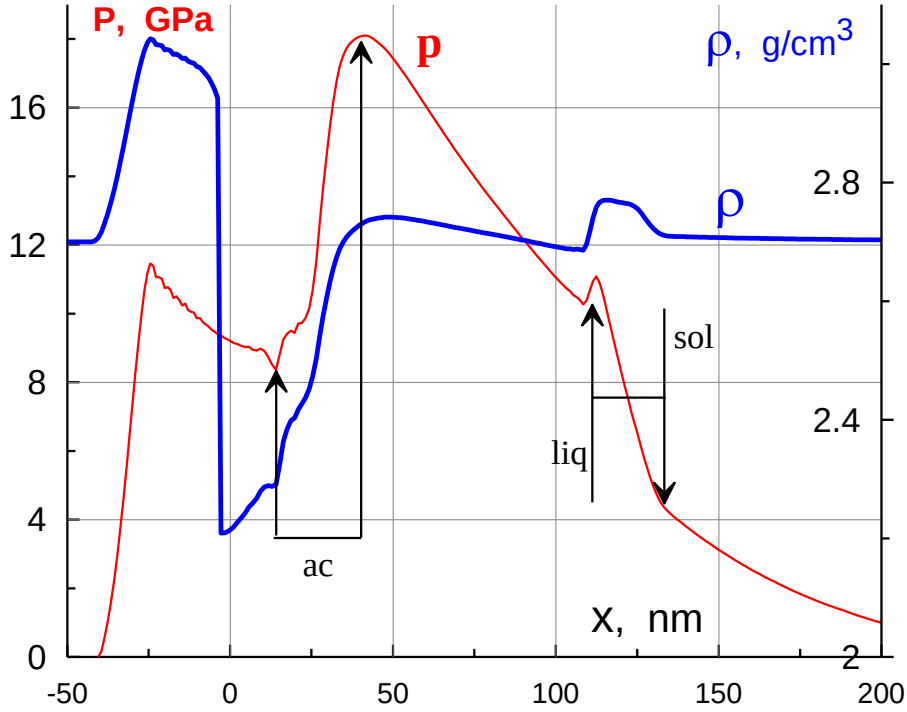

Fig. 5. Formation of compression wave due to absorption of pump pulse in a skin-layer of Al at a glass-Al boundary. Duration of pulse is 100 fs; absorbed energy is $F_{abs}=130$ mJ/cm^2; the time instant shown is 5 ps after pump.

The left jump in Fig. 5 corresponds to a shock propagating to the left in glass (the blue curve is a density profile; density axis is at the right side of Fig. 5). The sharp density decrease near the point $x=0$ corresponds to the current position of the glass-Al boundary. This boundary slowly moves to the left side as a result of melting and expansion of Al which has much higher temperature. The arrows "ac" (acoustic) mark a rarefaction wave propagating into Al after decay of pressure jump at the initial position of a glass-Al boundary. This pressure jump is created by very short heating (100 fs) of Al. This is pressure jump between cold glass transparent to pump light and hot pressurized Al heated by absorption of part of pump light. In this simulation we neglect optical breakdown in glass. The well near glass-Al boundary in the density profile $\rho(x, t=5\,\text{ps})$ in Fig. 5 corresponds to hot molten Al which expands in volume when pressure decreases as the rarefaction "ac" runs to the right from this volume.

Contrary to the case of expansion in vacuum (middle and right parts in Fig. 2), in the case with glass (Fig. 5), preventing easy expansion, the pressure in Al behind rarefaction does not fall down to zero. This pressure is maintained by shock in glass. Amplitude of shock in glass equals approximately to a

half of pressure jump created by ultra-fast laser heating of Al. Shock in glass slowly decays during propagation. Slow decrease of pressure in the layer of molten Al allows additional expansion of hot melt. This expansion acts against decrease in time of pressure in melt. This action supports pressure and later in time produces rather long tail of rarefaction wave "ac" shown in early stage in Fig. 5.

Gradual spatial variation of pressure in the region between the pressure maximum (the right arrow "ac") and the melting front (the arrows "liq" and "sol") in Fig. 5 corresponds to the compression wave propagating to the right.

The right two kinks "liq" (liquidus) and "sol" (solidus) in Fig. 5 limit a two-phase liquid-solid layer between them. They appear as a result of the kinks in the dependence of Gruneisen parameter on temperature at the isochoric line (density is constant; this corresponds to very fast heating during the two-temperature state) passing through a melting curve [12]. It is remarkable, that in the case of much higher absorbed energy, than shown in Fig. 5, the "liq/sol" kinks still exist and that they transform into elastic shock at pressures ~10 GPa which correspond to intersection of isochoric line and melting curve at the (ρ, p) thermodynamic plane [1,13-15]. These pressures are much higher than the usual Hugoniot Elastic Limit (HEL) for shock waves in metals.

Steepening and breaking of compression wave

Evolution of compression wave during its propagation is shown in Fig. 6. Simple Riemann wave shown in Fig. 6 is formed as result of acoustic decay of pressurized layer created by short laser irradiation. In the case shown in Fig. 6, pressures and velocities are small in comparison with bulk modulus 180 GPa (Nickel) and sound velocity ≈ 4.5 km/s. Energy absorbed by Ni is 50 mJ/cm^2. These conditions correspond to glass-Nickel (the left configuration in Fig. 2) experiment described in paper [16], see also [14, 15]. The point $x = 0$ at the axis in Fig. 6 gives initial position of glass-Ni boundary. The wave is weakly non-linear because pressure is small in comparison with bulk modulus.

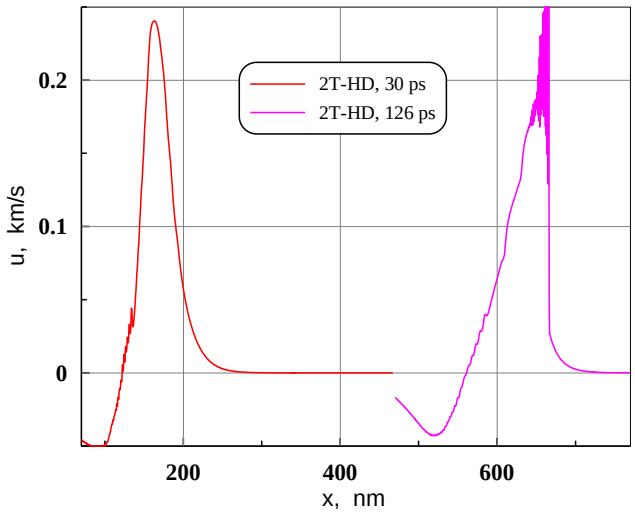

Fig. 6. Weakly non-linear transformation of simple Riemann wave during its propagation through Ni film. Non-linearity appears due to addition of flow velocity to sound speed and due to dependence of sound velocity on compression [17]. The non-linearity causes (i) steepening and breaking of the frontal side of the Riemann wave (see next Fig.) and (ii) stretching of the rear-side of the wave. The rear-side corresponds to rarefaction marked by arrows "ac" in Fig. 5.

Fig. 7 demonstrates how the Riemann wave overturns. Breaking of wave finalizes process of steeping of frontal side, see Fig. 6. Breaking corresponds to intersection of characteristics and formation of caustics. The breaking in Fig. 7 takes place between the instants shown in Fig. 6. Oscillations behind the shock front in Fig. 7 are connected with the scheme of numerical integration of two-temperature hydrodynamic (2T-HD code) equations. We use Lagrangian grid with steps 0.5-1 nm and Samarsky-Popov approach [18]. The shock front cuts the overturned profile to two parts (UAM and MRD) with equal surfaces [17]. The overturned profile is shown by red curve in Fig. 7. Amplitude DU of a jump in Fig. 7 first increases (compare instants 100 and 126 ps in Figs. 6, 7) as the jump overruns the precursor produced by fast electron heat conduction wave at the two-temperature stage [5, 12]. And second, the amplitude DU slowly decreases as rarefaction, sitting at the shock front, reduces the jump DU. At this stage, the shock profile takes a triangular shape. The profile for 126 ps shown in Fig. 6 is an example of such shape.

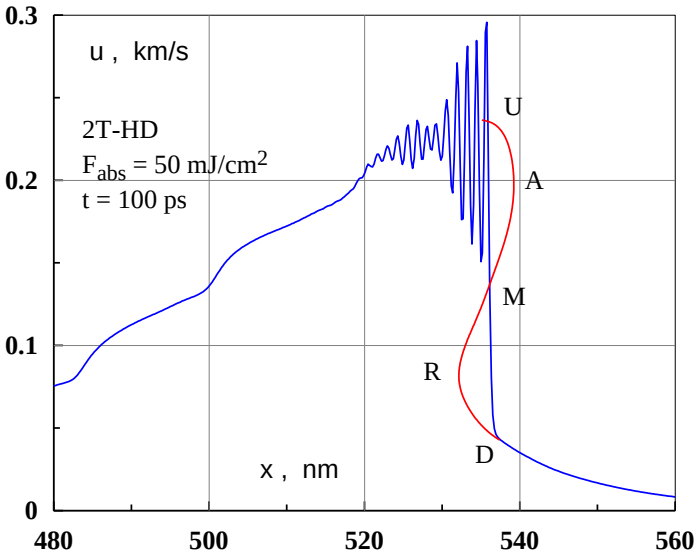

Fig. 7. Breaking of Riemann wave shown in previous Figure. Shock is accompanied by numerical oscillations.

Arrival and reflection of triangular shock from rear-side

Propagation of shock shown in Fig. 6 ends when the shock arrives at the rear-side of metal film. We are interested to consider material strength during reflection of shock from the metal-vacuum boundary. This is the case shown in the left part of Fig. 2. Arrival of wave sets the boundary in motion [4-7, 12]. Shift of the boundary as function of time is recorded by probe pulses shown in Fig. 2. Comparison of numerical and experimental results allows obtaining valuable information about elastic-plastic transformation and material strength [1, 3-7, 12-16, 19].

Material strength and its dependence on deformation rate and on temperature in case of melt

There is a unique opportunity to study influence of deformation rate $\dot{V}/V$ on material strength σ^* at very high values of $\dot{V}/V$ near the atomistic end [3-7] of the range of $\dot{V}/V$ (just 2-3 orders below the Debye frequency). This opportunity is connected with femtosecond lasers [3-7, 12-15, 19]. Results for Al and Au are shown in Fig. 8. This Figure in case of Al compares our results at the far right end of the $\dot{V}/V$ axis with results obtained with more usual techniques. The Al single crystal and AD1 dots correspond to the explosive experiments. They are taken from [20]. The two dotted curves present Eliezer et al. laser experiments with nanosecond laser pulses [21]. The two empty squares give the local values of σ and $\dot{V}/V$ for Al crystal at the instant just before beginning of the

subsequent fragmentation at the rear-side for $F_{abs} = 1.7F_{abs}|_{abl}$ and $F_{abs} = 5.2F_{abs}|_{abl}$. They are obtained with our molecular dynamics (MD) embedded atom method (EAM) potential for Al. This potential is adjusted to reproduce behavior of matter at large deformations. The corresponding acoustic approximations calculated from the rear-side velocity decrease are indicated by the two crossbucks. The filled black square represents the local values (in the point of future spall) for the EAM potential of Mishin et al. [22] with $F_{abs} = 2F_{abs}|_{abl}$ which is stronger than our optimized EAM potential. The limiting strength $\sigma_{\max}$ for Al marked with the horizontal straight corresponds to the uniform 3D expansion of Al crystal in our EAM potential. In the case of the uniaxial stretching the strength $\sigma_{\max}$ depends on the direction of stretching.

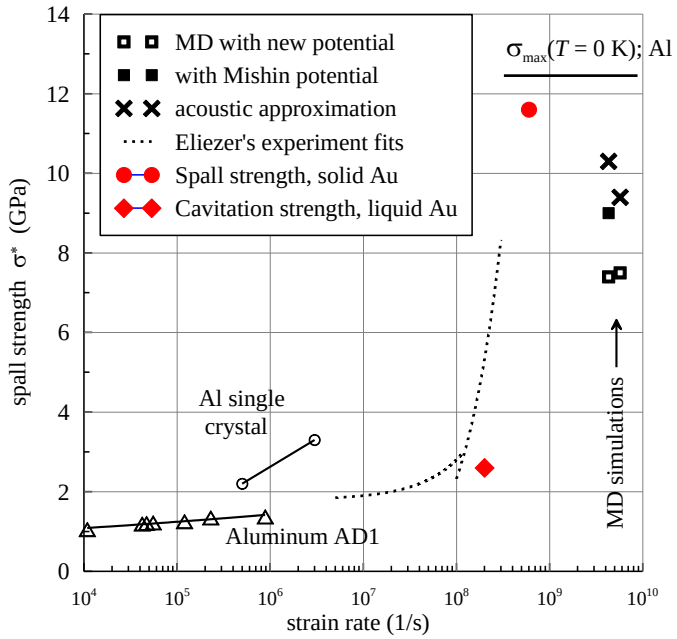

Fig. 8. Hardening of Al relative to the stretching rate $\dot{V}/V$. Comparison of MD data for Al with data for smaller rates $\dot{V}/V$ known from literature. Results for ablation (red diamond) and spallation (red square) of gold [6] are also shown. Due to heating and melting of Au the value of σ^* decreases in comparison with crystal. At the ablation threshold cavitation in Au begins near the melting front. During adiabatic expansion the melt around the future cavity cools down. Simulation shows that cavitation begins in the supercooled liquid Au ≈ 100 K below the triple point temperature.

Dependence of σ^* on temperature for Al is shown in Fig. 9. This dependence is obtained from MD simulation [19]. Results agree with our experimental measurements [4].

Summary

Detailed description of femtosecond experiments is presented. Such experiments and theoretical modeling allow us to look into processes from atomic time scale to meso-scales and to estimate temporal and pressure dependence of elastic-plastic transformation rates. Valuable data about material strength have been obtained. These data correspond to the extreme case at the highest possible deformation rates when matter is still may be described as condensed matter.

Authors (NAI, SIAsh, VAK, SIAn, MBA) acknowledge support from RFBR grant No. 10-02-00434-a

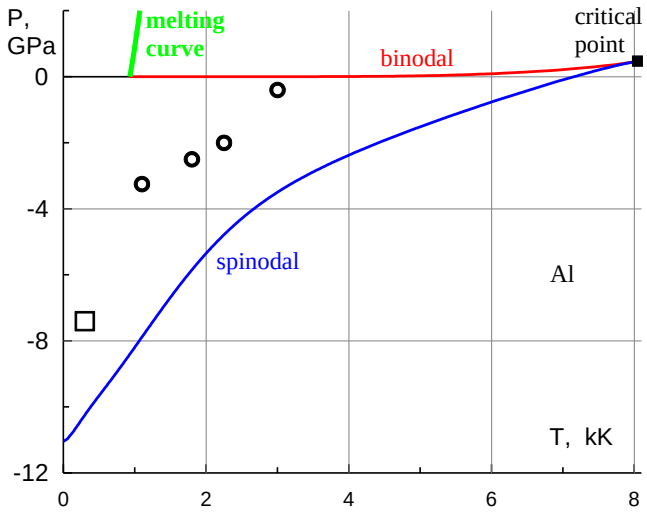

Fig. 9. Decrease of strength σ^* with increase of temperature of liquid Al. There is still significant gap between values of σ^* and the spinodal curve even at our very high deformation rates (see previous Figure).

References

[1] N.A. Inogamov, V.V. Zhakhovsky et al.: JETP Lett. Vol. 93(4) (2011), p. 226
[2] R. Evans, A. D. Badger, F. Falliès, M. Mahdieh et al.: PRL Vol. 77 (1996), p. 3359
[3] S. I. Ashitkov, M. B. Agranat, G. I. Kanel' et al.: JETP Lett. Vol. 92 (2010), p. 516
[4] S. I. Ashitkov, N.A. Inogamov, P.S. Komarov et al: Santa-Fe, HPLA-2012 Proc. (accepted)
[5] M.B. Agranat, S.I. Anisimov, S.I. Ashitkov et al.: JETP Lett. Vol. 91 (9) (2010), p. 471
[6] B.J. Demaske, V.V. Zhakhovsky, N.A. Inogamov, I.I. Oleynik: PRB Vol. 82 (2010), 064113
[7] V.V. Zhakhovskii, N.A. Inogamov et al.: Appl. Surf. Sci. Vol. 255 (2009) 9592
[8] V.H. Whitley, S.D. McGrane et al.: J. Appl. Phys. Vol. 109 (2011), p. 013505
[9] J.C. Crowhurst, M.R. Armstrong, K.B. Knight et al.: PRL Vol. 107 (2011), 144302
[10] N.A. Inogamov, Yu.V. Petrov: JETP Vol. 110(3), (2010), 446
[11] N.A. Inogamov, Yu.V. Petrov, V.A. Khokhlov et al.: Santa-Fe, HPLA-2012 Proc. (accepted)
[12] N.A. Inogamov, V.V. Zhakhovskii et al.: Contrib. Plasma Phys. Vol. 51 (2011), p. 367
[13] N. Inogamov, V.A. Khokhlov, Yu.V. Petrov, S.I. Anisimov, et al.: Eds. Tracy Vogler and Mark Elert. Shock Compression of Condensed Matter – 2011. AIP Conf. Proc. Vol. 1426, pp. 909-912 (2012); doi: 10.1063/1.3686425
[14] B.J. Demaske, V.V. Zhakhovsky, N.A. Inogamov et al.: *ibid*, pp. 1163-1166
[15] B.J. Demaske, V.V. Zhakhovsky et al.: Santa-Fe, HPLA-2012 Proc. (accepted)
[16] K.T. Gahagan, D.S. Moore, D.J. Funk et al.: PRL Vol. 85 (2000), p. 3205
[17] L.D. Landau and E.M. Lifshitz: *Fluid Mechanics* (Pergamon 1987)
[18] А.А. Самарский и Ю.П. Попов: *Разностные методы решения задач газовой динамики* (Наука 1992)
[19] M. B. Agranat, S.I. Anisimov, S.I. Ashitkov et al.: JETP Lett. Vol. 91 (9) (2010), p. 471
[20] G.I. Kanel, S.V. Razorenov, and V.E. Fortov: *Shock-Wave Phenomena and the Properties of Condensed Matter*. (Eds.) L. Davidson, Y. Horie. (Springer 2004).
[21] S. Eliezer, E. Moshe, and D. Eliezer: Laser and Particle Beams Vol. 20 (2002), p. 87
[22] Y. Mishin, D. Farkas, M.J. Mehl et al.: Phys. Rev. B Vol. 59 (1999), p. 3393